Bilinear stiffness and bimodular Poisson's ratio in cylindrical sinusoidal lattices through topology morphing

Venkatesh Sundararaman [a,b,*], Matthew P. O'Donnell [c], Isaac V. Chenchiah [d], Paul M. Weaver [a,b]

[a] *Bernal Institute, School of Engineering, University of Limerick, Limerick, Ireland*
[b] *Bristol Composites Institute (CoSEM), University of Bristol, Bristol, UK*
[c] *School of Engineering, University of the West of England, Bristol, UK*
[d] *School of Mathematics, University of Bristol, Bristol, UK*

ARTICLE INFO

ABSTRACT

Bilinear elastic behaviour allows structural designs to respond in either a stiff or compliant manner depending on the load. Here a cylindrical sinusoidal lattice structure is described that stiffens beyond a certain load. When subjected to axial compression, the lattice can undergo a topological transformation by forming contact connections. This topology change involves a transition from rectangular-like unit cells to kagome-like unit cells, associated with an approximately fourfold increase in stiffness. The lattice exhibits negative Poisson's ratio with a step-change from ≈ -0.66 to ≈ -0.23 prior to and during contact formation, respectively. After contact formation, it displays a nonlinear Poisson's ratio behaviour. The mechanics underpinning these behaviours are analysed using a combination of experiments and numerical modelling. A comparison with similar planar lattices reveals the effect of the global topology of the lattice (e.g. planar, cylindrical) on the unit cell-level topology morphing. The proposed topology-morphing cylindrical sinusoidal lattice introduces new design possibilities in the application-rich context of tubular structures with nonlinear mechanical properties.

1. Introduction

Cylindrical lattices have received increased interest in recent years owing to their advantageous properties. These include low weight [1, 2], shock [3,4] and energy absorption [5–10] capabilities, negative Poisson's ratio (NPR) [11–14], and extension- [15]/compression-twist coupling [16–20], making them suitable for diverse applications in aerospace [21–25], automotive [26,27], biomedical engineering [28–32], and soft robotics [33–35]. These lattices are constructed using a variety of microstructural unit cell designs [36], which impart the aforementioned macroscopic mechanical properties, while also allowing for the tailoring of these properties by tuning their geometric parameters. Wang et al. [26] utilised a NPR structure within a jounce bumper to improve automotive suspension systems. The study reported that NPR jounce bumpers had excellent viscoelastic properties, effectively absorbing impact energy due to their high damping capacity. Moreover, these bumpers exhibited mechanical behaviour similar to conventional ones, but with a smoother load-displacement curve, which could enhance the vehicle's performance by reducing noise vibration, and harshness. Inspired by the shape of a parrot's beak, Hamzehi et al. [10] pro-

posed zero Poisson's ratio cylindrical metamaterials which absorb and dissipate energy per unit of mass at high compressive strains without global buckling. Using finite element (FE) analysis and 3D-printed specimens, they demonstrated bistable deformation patterns including friction-based and interlocking mechanisms and also explored its full reversibility upon a heating–cooling process.

Several studies have investigated cylindrical lattices for use as biomedical stents [28–32]. Stents play a crucial role in the treatment of coronary artery disease and esophageal cancer, which are among the leading global causes of mortality [37]. Since certain arteries deform auxetically when simultaneously subjected to circumferential strain and wall shearing due to blood flow [38], the auxetic behaviour of cylindrical lattice structures can reduce deformation incompatibility with blood vessels and this could make them more suitable for angioplasty and oesophageal stent applications. Ali et al. [28,29] suggest that auxetic oesophageal stents with anisotropic mechanical behaviour can be more compatible with the multi-layered oesophageal wall, which exhibits nonlinear anisotropic mechanical response. Geng et al. [30] studied a 3D-printed cylindrical stent with chiral unit cells and demonstrated that its negative Poisson's ratio can be tailored using unit cell de-

---

sign parameters. Clinical stents should also possess high circumferential strength and bending flexibility to function effectively [39]. Jiang et al. [31] studied the radial mechanical performance of cylindrical sinusoidal lattice-based stents using FE analysis and experiments performed on 3D-printed prototypes. These auxetic tubular lattices exhibited a 72.7% increase in ductility compared to conventional diamond tubular structures. The study also reported that the beam depth-to-length ratio of sinusoidal ligaments significantly improves radial stiffness and peak load, while the amplitude ratio increases ductility. In another study [32], they analysed the bending behaviour, demonstrating that these cylindrical sinusoidal lattices exhibit highly compliant behaviour, resulting in an 85.4% increase in ductility compared to conventional diamond tubular lattices.

Many of these studies primary focus concerns improving/tailoring auxeticity, energy absorption and mechanical performance of cylindrical lattice designs. However, there is a growing acceptance of using nonlinear elastic behaviour in large-deformation (geometrically non-linear) components to optimise performance. Examples of this approach can be found across different length scales, including helical lattices [22,40–42], compliant mechanisms [43,44], and architected materials [45–47].

The potential benefits of geometric nonlinearity can be exploited further by allowing structural connectivity to adapt to better meet multiple operational requirements [48–54]. This reconfiguration establishes alternative load paths within the structural system, resulting in fundamentally different response modes, such as transitioning from high-compliance to high-stiffness behaviour. The formation of new connections leads to a new structural topology, a concept distinct from the more conventional approach of altering geometric shape alone. In architected materials, self-contact between unit cells often indicates the material transitioning into a plastic regime. [8,55–59]. However, with careful tuning of the design, self-contact can occur whilst remaining in an elastic regime as demonstrated in the study of topology morphing lattice structures [50,54]. Recent studies on metamaterials have attempted to achieve topological transformation using external actuators and materials to reshape the structure into a different topology, thus increasing system complexity [48,60,61]. In contrast, our approach achieves the topology transformation passively as a result of the applied load in isolation. This offers a new method for designing structures capable of morphing their topology, suitable for applications involving energy absorption initially and load carrying under large strains. The structure is designed to remain elastic with predictable nonlinear responses.

The topology-transformation of interest here is from rectangular unit cells to kagome unit cells, as studied in [50] for planar lattices. This topology change increases the compressive and shear stiffness approximately fourfold. Kagome-like lattice structures, within an intermediate density range, exhibit enhanced shear modulus compared to triangular-like (stretching-dominated) and hexagonal-like (bending-dominated) lattice structures. Moreover, they possess favourable transport and heat-dissipation properties, improved mechanical strength, and ease of fabrication [62].

Here, the potential benefits of elastic tailoring through reversible topology transformation are demonstrated in the context of cylindrical lattices, which arise in a wide range of physical systems and applications. In particular, the demonstration of bilinear elastic behaviour extends previous research on topology morphing in planar sinusoidal lattices [50] to cylindrical sinusoidal lattices. Unlike planar lattices, cylindrical lattices do not possess traction-free lateral boundaries. This closed geometry can induce out-of-plane flexure (torsion) in the beams, leading to a distinct response compared to planar lattices. Consequently, another key contribution of our work is physical insight into the differences in the elastic response of planar and cylindrical geometries, thus aiding in the development of tailored elastic responses.

Outline of the paper. This paper proceeds as follows: Section 2 provides a brief overview of topology morphing planar sinusoidal lattices
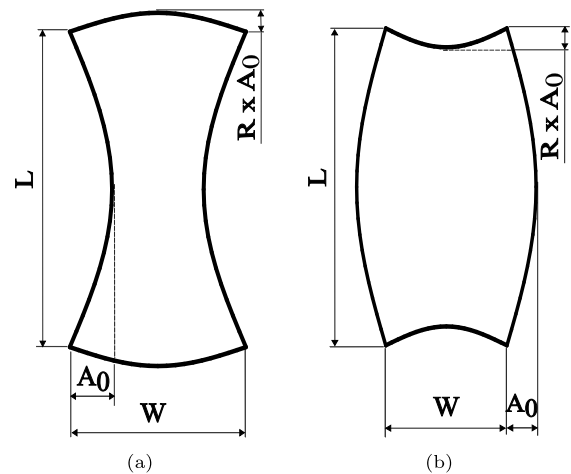
Fig. 1. (a) A sinusoidal unit-cell with a pair of concave sides (vertical) and a pair of convex sides (horizontal). (b) A sinusoidal unit-cell with a pair of convex sides (vertical) and a pair of concave sides (horizontal). A_0 is the amplitude of the vertical sinusoidal beam and L its half-wavelength; RA_0 is the amplitude of the horizontal sinusoidal beam and W is its half-wavelength. This figure is reproduced from [50].

as discussed in [50]. Section 3 introduces the cylindrical sinusoidal lattice, including details of the supporting FE analysis and the 3D-printed prototypes. Section 4 discusses the bilinear stiffness behaviour of the lattice by analysing its buckling and nonlinear static behaviour under axial compression. Section 5 compares the behaviour of the cylindrical lattice with that of the planar lattice. Finally, Section 6 summarises the key contributions of this study and its implications for future work.

2. Topology morphing planar sinusoidal lattice - an overview

The ability to control desirable topology morphing in an analogous planar sinusoidal lattice system has been demonstrated by Sundararaman et al. in [50]. Such a planar sinusoidal lattice comprises alternatively arranged unit cells, each containing pairs of concave and convex sinusoidal beams, as shown in Fig. 1. This cell arrangement gives rise to a checkerboard pattern (as seen in Fig. 2a). The vertical sinusoidal beams are characterised by an 'amplitude ratio', A_0/L, where A_0 is the amplitude and L is the half-wavelength. Horizontal beams have a half-wavelength of W and an amplitude of RA_0, where $R = W/L$ is the unit cell aspect ratio. Note that the amplitude-to-half-wavelength ratios are equal for the vertical and horizontal beams, and the corners of unit cells form right angles.

The design philosophy is that, upon sufficiently large axial compression, contacts are formed between vertical sinusoidal beams within unit cells that possess concave vertical beams, as illustrated in Fig. 2b. Such contacts change the topology of the lattice from rectangle-like to kagome-like unit cells. The compressive load at which contacts would occur (by inducing the preferred deformation mode shown in Fig. 2b) is called the 'contact load'. The contact load depends on the amplitude ratio.

For small amplitude ratios, the lattice buckles globally at a load smaller than the contact load, thereby precluding intra-cell contact. This global buckling load also depends on the amplitude ratio. However, when a critical amplitude ratio, $(A_0/L)_{\text{crit}}$, is exceeded, the contact load becomes less than the global buckling load, thus enabling the desired topology change. Such amplitude ratios are referred to as super-critical amplitude ratios.

The critical amplitude ratio depends on the three hierarchical geometric parameters of the lattice (i) slenderness ratio of the lattice (ii) slenderness ratio of the unit cell and (iii) slenderness of the vertical sinusoidal beams. These geometric parameters along with super-critical
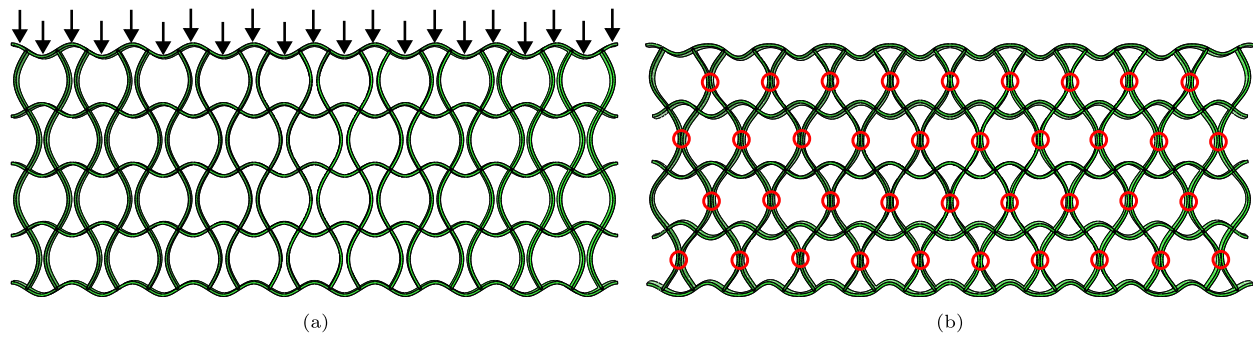
Fig. 2. Planar sinusoidal lattice. (a) Undeformed state. The two sinusoidal unit-cells shown in Fig. 1 are arranged in a checkerboard pattern. (b) Topology-morphed state under compression. Circles in red indicate the contact between the vertical sinusoidal beams.
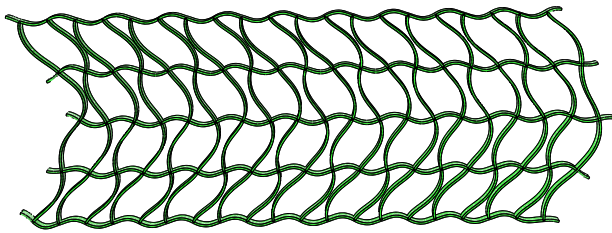

Fig. 3. Global buckling mode of a planar sinusoidal lattice under axial compression, obtained from linear buckling FE analysis.

Table 1
Thickness of 3D-printed sinusoidal beams.

Amplitude ratio, A_0/L	Thickness (mm)
0.12	1.03
0.15	1
0.18	0.99
0.19	1.11
0.20	0.96

amplitude ratio also enable stiffness tailoring of the sinusoidal lattice, as studied in [50].

3. Topology morphing cylindrical sinusoidal lattice

Building on the understanding gained of topology morphing behaviour in planar sinusoidal lattices, this phenomenon is now explored in cylindrical sinusoidal lattices.

Consider, conceptually, a planar sinusoidal lattice with $N_x = 20$ horizontal unit cells, $N_y = 4$ vertical unit cells and overall width πD. This planar lattice is rolled to form a cylindrical sinusoidal lattice with mean diameter D, as illustrated in Fig. 4. The lattice parameters $L = 24$ mm, $W = \pi D/N_x = 12.57$ mm, $D = 80$ mm, $b = 5$ mm (out-of-plane or radial depth) and $t = 1$ mm (wall thickness) remain constant for all the lattices considered in the study with only amplitude ratio and out-of-plane depth being varied. The geometry under consideration offers sufficient insight into the underlying physics of lattice behaviour and thus serves as a representative model of the general system. Fig. 5 illustrates the desired topology-morphing behaviour.

3.1. Finite element analysis

Finite element simulations in Abaqus/Standard 2020 [63] were performed to characterise the linear buckling and nonlinear axial compression behaviours of the lattice.

A linear elastic material model representing multi jet fusion (MJF) 3D-printed Polyamide 12 (PA 12) was used with the following material parameters [64]: Young's modulus $E = 1800$ MPa, Poisson's ratio $\nu = 0.4$ [65], ultimate stress $\sigma_y = 48$ MPa, density $\rho = 1010$ kg/m^3. Four-noded quadrilateral shell elements (S4R) [63] with an average element length of 0.6 mm were used to mesh the lattices in a structured manner. This mesh ensured a convergence tolerance of approximately 0.1% on the load of the first buckling mode, and it was also used for the nonlinear static analysis.

The lattice was compressed between a pair of rigid surfaces which replicates the loading conditions of the test setting. The reference node on the bottom rigid surface was fully constrained while the top rigid surface was constrained to displace vertically. The penalty method [63]

with a friction coefficient of $\mu = 0.15$ was used to model contact between the rigid surfaces and the lattice. This value allowed close simulation of the lattice behaviour observed during experiments, specifically the outward expansion (sliding) of the lattice on rigid surfaces due to its NPR behaviour. A friction coefficient of $\mu = 0.4$ was used between the sinusoidal beams to study the general behaviour of the lattice.

If the lattice deformed with radial symmetry, there would be no post-contact sliding between the sinusoidal columns. Nevertheless, to account for deformations that break symmetry, the FE simulations were performed with friction coefficients of $\mu = 0.2, 0.4, 0.6, 0.8$ and 1. However, these solutions were, in fact, symmetric, and thus the friction coefficient between the sinusoidal beams does not affect the post-contact behaviour of the lattices, before global buckling. This effect is shown in Figs. 11–14 in Section 4.2.

3.2. 3D-printed prototypes

To validate the behaviour observed in FE analysis, five prototype cylindrical lattices with amplitude ratios 0.12, 0.15, 0.18, 0.19 and 0.20 were fabricated using MJF 3D printing process [66]. These amplitude ratios were sufficient to understand the general behaviour of the proposed concept. A HP 3D 4200 Printer was used to fabricate the samples with HP PA 12 material, with the same properties [64] as used in the FE simulations (Section 3.1).

The MJF process produces parts with near-isotropic material properties [67]. It does not require support structures which is particularly important for fabricating the cylindrical sinusoidal lattices due to the orientation of the printing axis and 3D beam curvatures. For example, initial fabrication attempts using fused deposition modelling had very poor layer-to-layer continuity. An example of the MJF lattice is shown in Fig. 6.

The measured mean thickness of the 3D-printed sinusoidal beams deviated from the design thickness of 1 mm, as listed in Table 1. The error between the design and fabricated thickness was less than 5%, except for the lattice with $A_0/L = 0.19$ in which the deviation was 11%. Nevertheless, for an accurate comparison, the thickness in the FE analysis was adjusted to match the thickness of the fabricated samples.
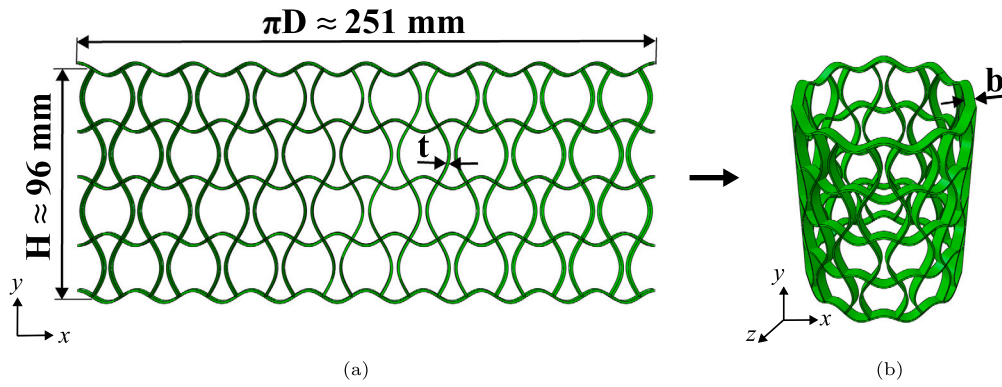
Fig. 4. (a) A planar sinusoidal lattice consisting of $N_x = 20$ unit-cells in the horizontal direction and $N_y = 4$ unit-cells in the vertical direction. (b) A cylindrical sinusoidal lattice formed by rolling the planar lattice in (a).
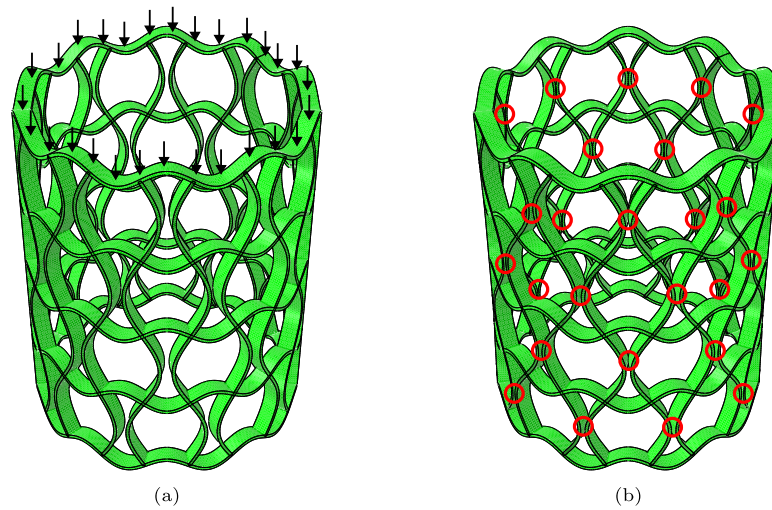

Fig. 5. Cylindrical sinusoidal lattice (a) Undeformed and (b) topology morphed under compression through contact connections (circles in red indicate the contact between the vertical sinusoidal beams).
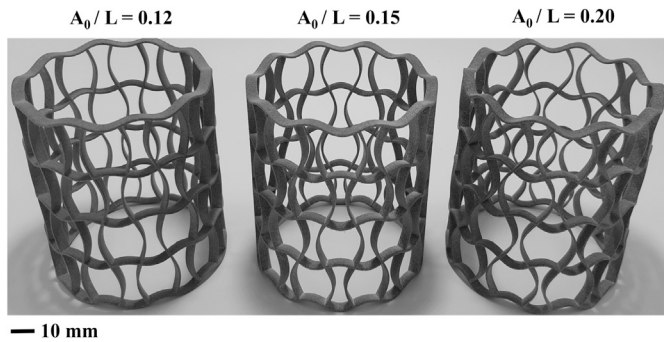

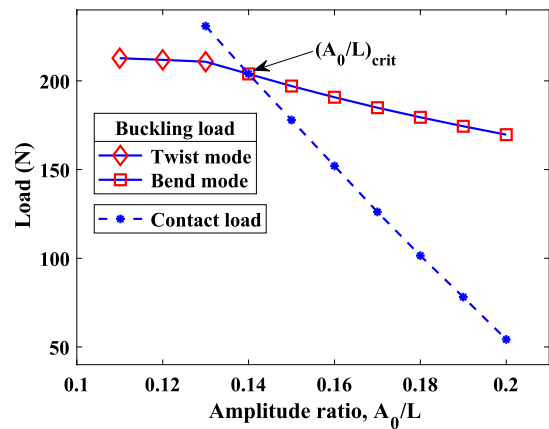**Fig. 6.** MJF 3D-printed cylindrical lattices.

Fig. 7. Global buckling load versus contact load of the cylindrical lattice for various amplitude ratios obtained from FE analysis.

4. Cylindrical sinusoidal lattice behaviour

4.1. Bilinear stiffness

The importance of the critical amplitude ratio for planar lattices has been identified previously and has informed our present approach [50]. The first step in investigating the behaviour of cylindrical lattices is to estimate the global buckling load and the contact load for various amplitude ratios. Fig. 7 illustrates, through FE analysis, that as the amplitude ratio increases, both the global buckling load and the contact load decrease. (The contact load for the lattice with an amplitude ratio of 0.13 was obtained by inducing the corresponding deformation mode

in the FE analysis.) This decrease in load is a result of the increase in the amplitude ratio, which reduces the axial and bending stiffness of the sinusoidal beams, as explained in [50].

In fact, cylindrical lattices exhibit two distinct fundamental global buckling modes. The first is the twisting mode (see Fig. 8a), which occurs for small amplitude ratios such as 0.11, 0.12, and 0.13. However, at amplitude ratios of 0.14 and beyond, the bending mode (see Fig. 8b) becomes dominant. This shift in buckling behaviour at an amplitude ra-
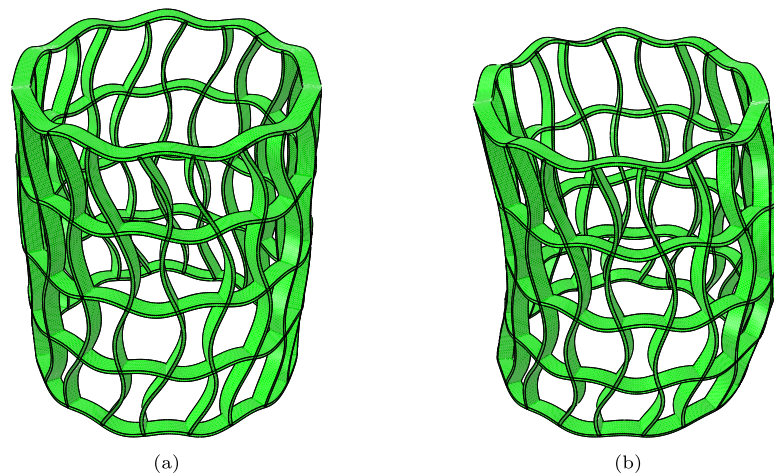
Fig. 8. Global buckling modes of cylindrical lattices (a) Twisting mode and (b) Bending mode.
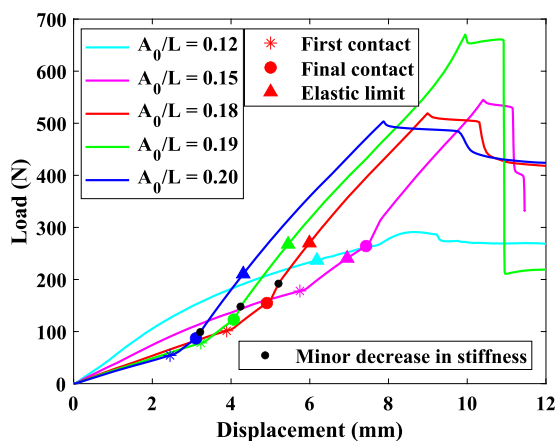

Fig. 9. Load versus displacement of the cylindrical lattice under compression for various amplitude ratios, obtained from FE analysis.

tio between 0.13 and 0.14 can be observed as a change in slope in the buckling load curve, Fig. 7.

The shift in global buckling from twisting to bending mode can be readily explained. When the amplitude ratio is small, the bending stiffness of sinusoidal beams is relatively higher. Specifically, those vertical sinusoidal beams which are perpendicular to the global bending axis prevent the lattice from globally bending due to their larger second moment of area about the global bending axis. As a result, these vertical sinusoidal beams tend to twist, i.e. they bend along the circumferential direction, causing an overall twist of the lattice. However, as the amplitude ratio increases, the bending stiffness of the vertical beams decreases. This decrease in stiffness causes the vertical beams to start bending about the global bending axis.

The global buckling load and the contact load become equal at the critical amplitude ratio of 0.14.

Fig. 9 presents the load-displacement curves under compression for super-critical amplitude ratios. As the amplitude ratio increases the stiffness of the lattices decreases due to the reduction of the bending stiffness of the sinusoidal beams, as discussed in Sundararaman et al. [50]. The increase in amplitude ratio also results in a decreased compression requirement for achieving contact between the sinusoidal beams, because the gap between the sinusoidal beams within a unit cell decreases as the amplitude ratio increases.

The lattices exhibit an approximately linear response until the occurrence of the first contact, indicated by '∗' in the figures. Here, 'first contact' refers to the first occurrence of self-contact in the lattice. This

contact occurs simultaneously within all unit cells in the middle two layers. Following first contact, the stiffness continues to increase linearly until contacts within the unit cells at the top and bottom layers (boundary layers) are established. Contacts in unit cells at boundaries are formed later due to their relatively higher stiffness provided by the boundary conditions. Once contacts in all unit cells (final contact) are established, the stiffness further increases linearly, signifying a transition in topology from a rectangle-like structure to kagome-like unit cells. The final contact is denoted by '•' in the figures.

Because the transition regime between the initial and final contacts is relatively small compared to the pre- and post-contact regimes, the behaviour of the lattice can be approximately characterised as bilinear. When the lattice is subjected to sufficient loading after the topology change, post-contact global buckling occurs. This global buckling phenomenon is characterised by a brief flat portion in the curves, followed by a drop in load, as shown in Fig. 9.

The solid triangles (▲) in Fig. 9, coloured to match the curves represent the elastic limit. Here, 'elastic limit' refers to the load at which the von Mises stress within the lattice reaches the ultimate material stress, σ_u. Typically, the maximum stress point is observed at the joints on the boundary layers as they flatten due to compression between rigid surfaces. The following discussion focuses on the elastic behaviour of the lattice.

For amplitude ratio 0.15, the first contact takes place within the elastic limit; however, contacts within all unit cells do not occur in this elastic region. For larger amplitude ratios, specifically 0.18, 0.19, and 0.20, final contact occurs within the elastic limit, resulting in a complete elastic transformation of the lattice topology. This topology change increases the compressive stiffness by approximately 3.82, 4.16 and 4.73 times for amplitude ratios of 0.18, 0.19 and 0.20, respectively. The magnitude of stiffness increase is larger for higher amplitude ratios because these lattices undergo a larger membrane effect due to the increased contact area with an increase in curvature. Fig. 9 shows a significant elastic regime after final contact for these amplitude ratios. A minor decrease in stiffness can be observed in the figure at displacements of 5.2 mm, 4.2 mm, and 3.2 mm, respectively, for these amplitude ratios, denoted by black dots on the curves. This decrease is attributed to a change in the deformation behaviour of the lattice. After the establishment of final contacts, the lattices exhibit a membrane effect with increased stiffness. However, under further compression, they energetically prefer to deform through out-of-plane flexure of the vertical beams. This out-of-plane flexural behaviour increases the contact area between the beams along the depth of the beams i.e. expanding from the inner to the outer edges.

Complete elastic transformation of the lattice topology would be possible also for amplitude ratios between 0.15 and 0.18 if a mate-
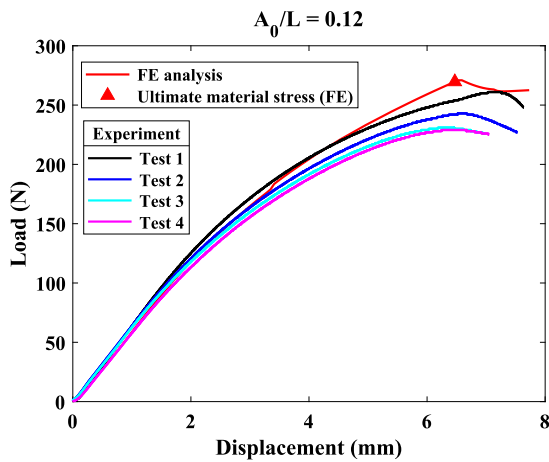
Fig. 10. Load versus displacement of the cylindrical lattice with amplitude ratio 0.12 under compression.

Fig. 11. Load versus displacement of the cylindrical lattice with amplitude ratio 0.15 under compression.

Fig. 12. Load versus displacement of the cylindrical lattice with amplitude ratio 0.18 under compression.

Fig. 13. Load versus displacement of the cylindrical lattice with amplitude ratio 0.19 under compression.

rial with a greater yield strain (than PA 12) were used. Moreover, bespoke multi-linear elastic stiffness responses can be achieved by tailoring the hierarchical geometric parameters. Based on the study of topology morphing sinusoidal planar lattices [50], the three key geometric parameters of the cylindrical lattice are expected to be: (i) the slenderness of the vertical sinusoidal beam, (ii) the ratio of vertical and horizontal sinusoidal beam stiffness, and (iii) the ratio of the cylindrical lattice aspect ratio (D/H) to the slenderness of the vertical beam, where H is the mean height of the lattice given by $L \times N_y$. Additionally, the out-of-plane or radial depth also influences the behaviour of the cylindrical lattice. For example, as the radial depth increases, the gap at the inner edges of unit cells decreases, which causes contacts to occur earlier than in the planar lattice with a uniform gap. The effect of radial depth on the load-displacement behaviour is discussed in Sections 5.3.

4.2. Experimental behaviour

To validate the behaviour of cylindrical lattices observed in the FE analysis, 3D-printed lattices with amplitude ratios of 0.12, 0.15, 0.18, 0.19 and 0.20 were tested under quasi-static compression. The compression tests were conducted at a displacement rate of 2 mm/min using a Tinius Olsen universal testing machine equipped with a 1 kN load cell.

To provide an accurate comparison the experimental results are compared with FE analysis that utilise the observed thickness of the fabricated specimens (see Table 1). These comparisons are presented in Figs. 10–14. However, the experiments are performed primarily to demonstrate the qualitative behaviour (bilinear response) of the proposed system and to validate the robustness of the FE model. Supplementary videos S1 to S3 show the compression behaviour of lattices during testing, corresponding to amplitude ratios of 0.12, 0.19 and 0.20, respectively.

The lattices were tested until post-contact global buckling, and FE results (see Fig. 9) demonstrate that some regions of the lattice would have undergone plastic deformation. The experimental tests were repeated four times for each amplitude ratio. The first test closely matches the FE results. A decrease in stiffness was observed for the subsequent tests, which can be attributed to the localised effects plastic deformation. This decrease is particularly evident for amplitude ratios of 0.12, 0.15, and 0.18.

For amplitude ratio 0.12, the lattice buckles globally before contacts occur in unit cells. This global buckling is reflected by the drop in load at an approximate displacement of 6.5 mm in the load-displacement curves shown in Fig. 10. For amplitude ratio 0.15, the lattice buckles globally before reaching the final contact point, except for the first test, see Fig. 11. This behaviour is explained, as supported by the FE anal-
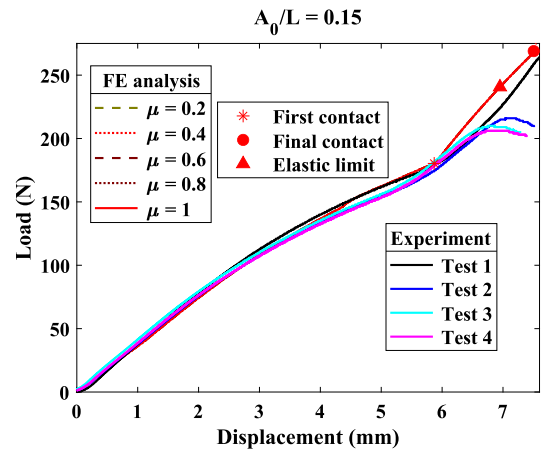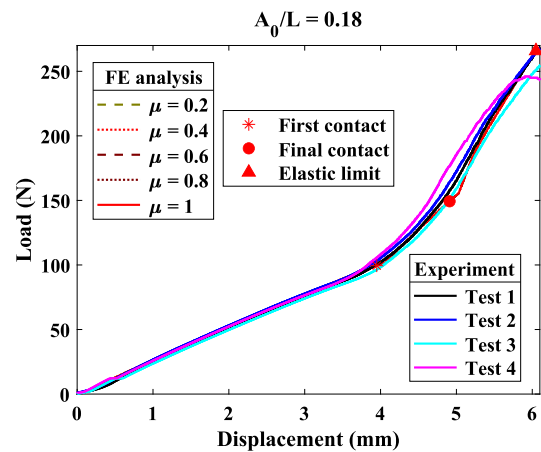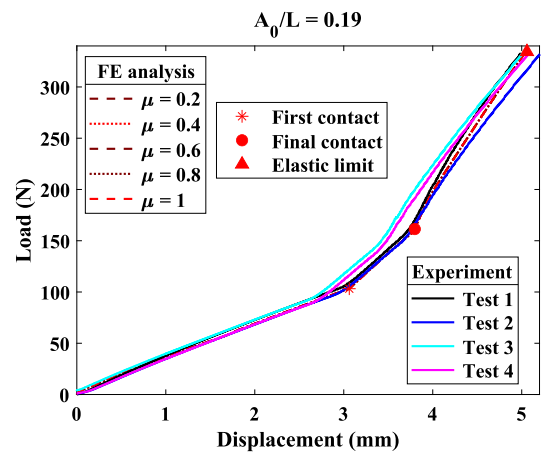
ysis, because the lattice reaches its elastic limit before final contact. Therefore, during the first test, the lattice would have sustained plastic damage in some locations, causing it to buckle at a reduced load.

For amplitude ratio 0.18, during the final test (Test 4 in Fig. 12), the lattice buckles globally near the elastic limit, because it had sustained plastic damage during its previous tests. However, it is noteworthy that
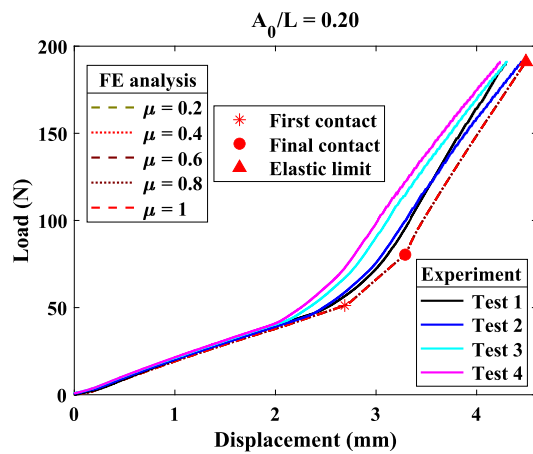
Fig. 14. Load versus displacement of the cylindrical lattice with amplitude ratio 0.20 under compression.

the FE results suggest that the plastic deformations are primarily local, and no visible physical damage or catastrophic failure was observed in the lattices. The repeated test results show reasonable consistency, especially for amplitude ratios 0.18, 0.19, and 0.20, as illustrated in Figs. 12, 13, and 14, respectively.

In addition to bilinear response, the cylindrical sinusoidal lattices also exhibit negative Poisson's ratio. Therefore, examining how changes in topology through contact interactions affect the NPR can offer valuable insights for system design.

4.3. Negative Poisson's ratio

Figs. 15a and 15b illustrate variations in mean radius and Poisson's ratio against axial compression, obtained from FE analysis for lattices with amplitude ratios of 0.18, 0.19, and 0.20. The mean radius is measured at the mid-circumferential sinusoidal ring of the lattice, while the (tangent) Poisson's ratio is calculated as the derivative of the nominal lateral-longitudinal strain curve. Points **A**, **B**, **C**, and **D** in both figures indicate transitions in the compressive response of the cylinder, discussed in detail in the following paragraphs.

*Until **B**.* After an initial compression of about 0.1 mm, contacts between the lattice and the rigid plates are established at point **A**. Subsequently, the mean radius undergoes an approximately linear decrease with compression until the first self-contact, which occurs due to the bending of both vertical and horizontal beams. Consequently, the Poisson's ratio remains approximately constant until first contact, with values of ≈ -0.67, ≈ -0.66 and ≈ -0.65 for amplitude ratios 0.18, 0.19 and 0.20 respectively. It can be noted that the absolute value of the Poisson's ratio decreases as the amplitude ratio increases. This happens because the greater amplitude ratio corresponds to an increased bending of beams, as discussed in Section 4.1.

B to first contact. At point **B**, the Poisson's ratio decreases (becomes more negative) by about 7%; the corresponding nonlinearity in the load-displacement curves is shown in the pre-contact regime of Fig. 9. This effect could be due to a change in the relative magnitudes of the axial (membrane) and bending behaviour of the beams.

First contact to final contact. The occurrence of first contact restrains the bending of vertical beams, leading to a decrease in the rate of decrease of cylinder radius with compression. As a result, the Poisson's ratio sharply increases, reaching ≈ -0.25, ≈ -0.22, and ≈ -0.21, respectively. Subsequently, the Poisson's ratio remains relatively constant until final contact (i.e. complete topology transformation) occurs. The

increased gap-to-contact for a smaller amplitude ratio results in the expected increase in compression required before first and final contact occurs.

*Final contact to **C**.* Now that the topology has transformed, and contacts established between vertical beams in all unit cells, further compression increases the bending resistance of the beams. The subsequent membrane-dominated response increases the mean radius by $\approx 0.02\%$ between final contact and point **C** in Fig. 15a. The membrane behaviour also explains the observed increase in stiffness upon final contact in the load-displacement curves (Fig. 9) in Sections 4.1 and 4.2. In this membrane-dominated regime, the lattice behaves more like a conventional material (i.e. less bending) and the Poisson's ratio increases to positive values of ≈ 0.08, ≈ 0.14 and ≈ 0.20, respectively. Higher amplitude ratios result in a larger peak Poisson's ratio due to the increased contact area associated with increased curvature of the beams. This explanation is further supported by the observation that higher amplitude ratios exhibit relatively larger increases in stiffness, as discussed in Section 4.1.

*From **C**.* From point **C**, the Poisson's ratio decreases sharply to negative values of ≈ -0.1, ≈ -0.16 and ≈ -0.24, respectively. This sharp change in Poisson's ratio happens because of the decrease in mean radius that is shown in Fig. 15a. Additionally, the load-displacement curves in Fig. 9 suggest the onset of out-of-plane flexural behaviour, characterised by a slight drop in stiffness upon increased compression after the final contact, as discussed in Section 4.1. (The black dots in Fig. 9 correspond to the points **C** in Fig. 15.) ratios. FE simulations corroborate this explanation by revealing that, as compression increases, the contact region between the vertical beams enlarges from inner edges to outer edges.

As the amplitude ratio increases, the compression range in which the lattices display a positive Poisson's ratio decreases. With higher amplitude ratios, there is a reduction in bending stiffness, and out-of-plane flexural behaviour of the vertical beams becomes energetically favourable at an earlier stage.

After this sharp drop at point **C**, the Poisson's ratio continues to decrease until the elastic limit, to values of ≈ -0.32, ≈ -0.32 and ≈ 0.23, respectively. This decrease is due to the nonlinear decrease in mean radius from point **C** as shown in Fig. 15a. A small jump in Poisson's ratio at point **D** could be attributed to a slight degree of nonlinearity in the mean radius versus compression curves, similar to that discussed for the decrease at point **B**. However, no significant changes in the deformation behaviour were observed at points **B** and **D** during FE simulations.

Summary of change in Poisson's ratio. The lattices experience an initial step-increase in Poisson's ratio upon first contact, followed by a linear decrease after a sharp decrease at point **C**. These changes coincide with notable alterations in the physical behaviour of lattices. Nonetheless, the mean radius change displays an approximate bilinear behaviour due to topology change, indicating the bimodular response of Poisson's ratio in these lattices. The close agreement between the FE and experimental load-displacement results, as presented in Section 4.1, demonstrates the robustness of the FE model. In particular, this close agreement suggests sufficient accuracy of Poisson's ratios estimated using FE analysis, even though they were not validated directly experimentally. However, the predicted synclastic deformed shapes of the cylindrical lattice, which result from NPR, were observed and are clearly shown in Fig. 16.

5. Comparison of cylindrical and planar lattices

5.1. Global buckling and contact load

A key motivation for this study was to characterise the geometrical transition from a two-dimensional planar to a three-dimensional cylindrical structure. Therefore, to understand the behavioural difference between these geometries, the behaviour of unrolled planar versions of
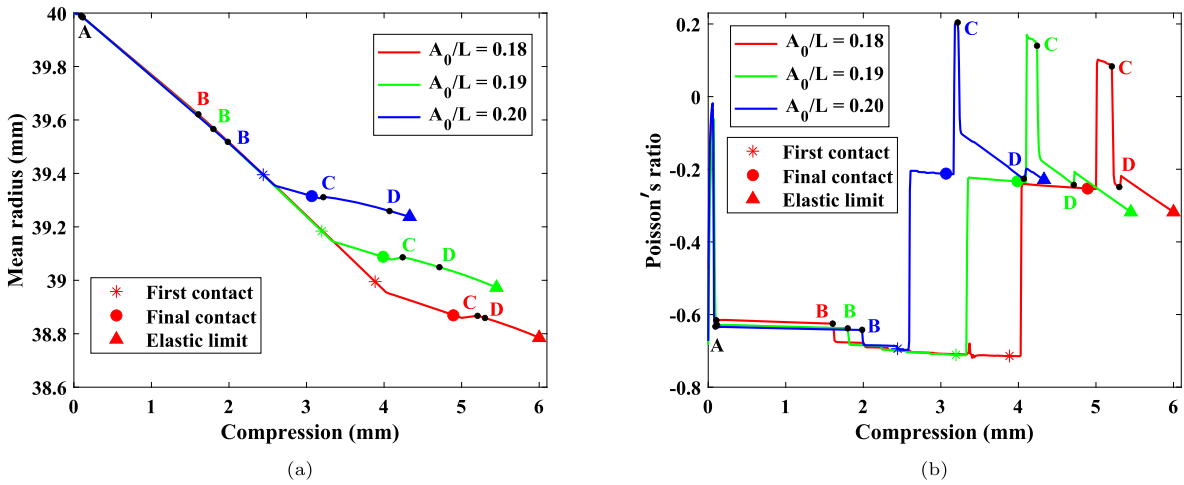
Fig. 15. (a) Mean radius versus compression and (b) Poisson's ratio versus compression of the cylindrical lattice for amplitude ratios 0.18, 0.19 and 0.20, obtained from FE analysis.
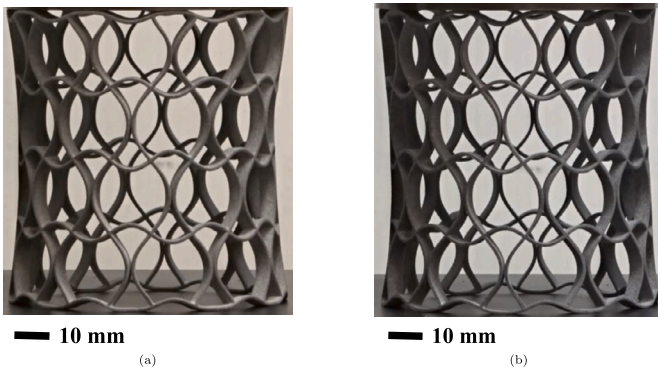

Fig. 16. Synclastic shapes of cylindrical sinusoidal lattice exhibiting negative Poisson's ratio behaviour under axial compression (a) $A_0/L = 0.19$ and (b) $A_0/L = 0.20$.
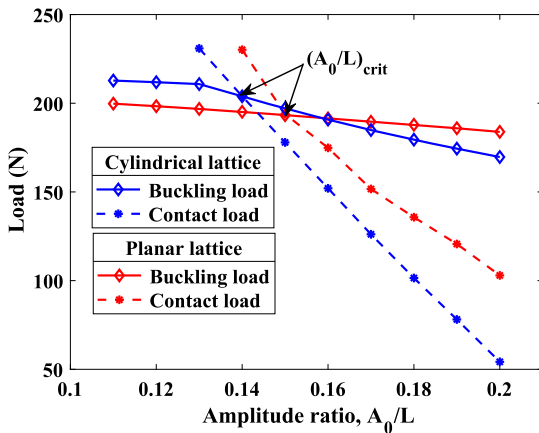

Fig. 17. Global buckling load versus contact load of the cylindrical and planar lattices, obtained from FE analysis.

the cylindrical lattices with the same geometrical parameters is investigated.

Fig. 17 shows the comparison of the global buckling and contact load (both obtained from FE analysis) of the planar lattice with that of the cylindrical lattice. Unlike the cylindrical lattice (see Fig. 3), the planar lattice exhibits only the lateral buckling mode as its fundamental buckling mode for all amplitude ratios. Hence, the decrease in global

buckling load against the increase in amplitude ratio appears relatively more linear. For amplitude ratios until 0.13 (i.e. for amplitude ratios with twist global buckling mode), the global buckling load of the cylindrical lattice is approximately constant and is higher than that of the planar lattice. However, beyond an amplitude ratio of 0.14 (i.e. for amplitude ratios with bending mode as their global buckling mode), the global buckling load linearly decreases and becomes less than that of the planar lattice at an amplitude ratio of 0.16. This decrease in the global buckling load of the cylindrical lattice suggests that the influence of the decreasing amplitude ratio is relatively larger in the case of the cylindrical lattice.

For all amplitude ratios, the contact load is larger for the planar rather than for the cylindrical lattice, because the planar lattice is stiffer reflecting the lack of twist deformation during bending of the sinusoidal beams. Also, the traction-free lateral boundaries of the planar lattice make it effectively stiffer than the cylindrical lattice. However, similar to the cylindrical lattice, the contact load follows an approximately linear decreasing trend with an increase in amplitude ratio. These effects in combination increase the critical amplitude ratio from 0.14 in the cylindrical lattice to 0.15 in the planar lattice.

5.2. Bilinear behaviour

As shown in Section 4.1, the cylindrical lattice exhibits bilinear elastic behaviour under compression for super-critical amplitude ratios of 0.18, 0.19, and 0.20. These amplitude ratios also fall into the super-critical range for the planar lattice. Fig. 18 compares the load-displacement behaviour of the planar lattice at these amplitude ratios with that of the cylindrical lattice. For all amplitude ratios, initial contact in cylindrical lattices occurs earlier than in planar lattices. This effect can be explained by considering the gap-to-contact response in the cylindrical lattice, between the inner edges (in the radial direction) of the vertical sinusoidal beams, being smaller than the uniform gap between the beams in the planar lattice. Therefore, in cylindrical lattices, contact initially occurs at the inner edges. As compression increases, the contact area gradually expands, progressing toward the outer edges of the beams.

For the planar lattice with an amplitude ratio 0.18 the elastic limit is reached before contacts occur in all unit cells. However, for an amplitude ratio 0.19 the elastic limit is reached immediately after the final contact. Increasing the amplitude ratio to 0.20, a significant second linear stiffness regime is observed after the final contact, i.e. after topology change. In this case, the stiffness increases by 6.88 times from that of its initial topology, which is greater than the increase observed in the
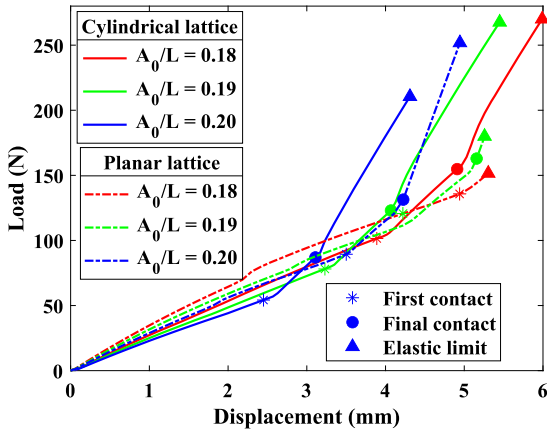
Fig. 18. Load versus displacement under compression for cylindrical and planar lattices with amplitude ratios 0.18, 0.19 and 0.20, obtained from FE analysis.
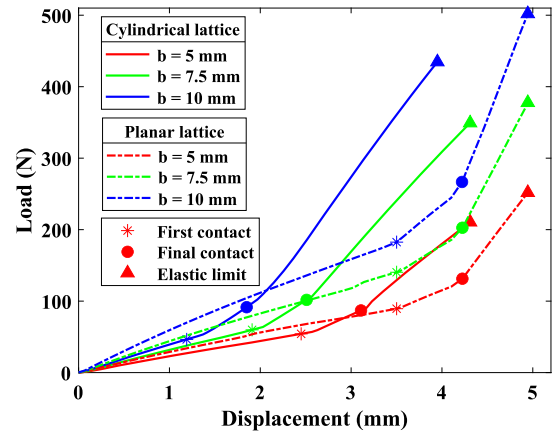

Fig. 20. Load versus displacement under compression for cylindrical and planar lattices with amplitude ratio 0.20 for various depths, obtained from FE analysis.
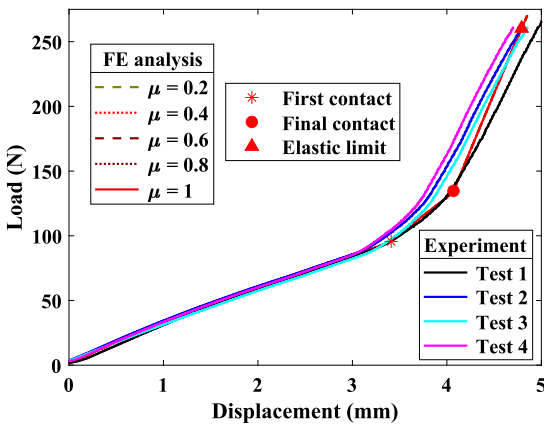

Fig. 19. Load versus displacement under compression for the planar lattice with amplitude ratio 0.20, obtained from FE analysis and experiment.

Fig. 21. Reaction moment about vertical axis versus compression of the cylindrical lattice with amplitude ratio 0.20 for various depths, obtained from FE analysis.

cylindrical lattice. Also, as shown in Fig. 18, the pre-contact stiffness of planar lattices is higher than that of the cylindrical lattices.

The larger stiffness in the initial and transformed topologies of the planar lattice results from the presence of traction-free lateral boundaries. These lateral boundary effects are not present in the cylindrical lattice. However, the nature of cylindrical geometry induces out-of-plane flexure of sinusoidal beams resulting in relatively lower stiffness compared to the planar counterpart. The effects of out-of-plane (or radial) depth on load-displacement and NPR behaviours are discussed in Sections 5.3 and 5.4, respectively.

To validate the FE results for the planar lattices, a 3D-printed planar lattice with an amplitude ratio of 0.20 was subjected to experimental testing under quasi-static compression using the same material properties as those used in Section 3.2. The actual thickness of the fabricated lattice was 1.03 mm. FE analysis was performed using this same thickness, and the resulting load-displacement behaviours are presented in Fig. 19. The close agreement between the FE and experimental results highlights the robustness of the FE model in accurately predicting planar lattice behaviour.

5.3. Effect of out-of-plane (or radial) depth

For a given out-of-plane (or radial) depth, the unit cells of the planar lattice possess a uniform gap between the sinusoidal beams. However, in the unit cells of the cylindrical lattice, the mean gap is greater than that between the inner edges but less than that between the outer edges. Hence, the radial (out-of-plane) depth of the cylindrical lattice influences its topology morphing behaviour.
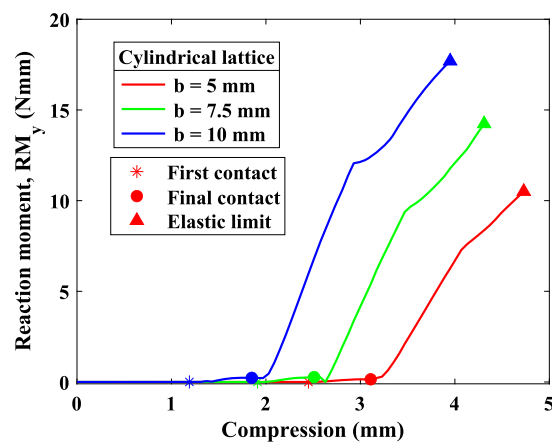
As the out-of-plane depth increases, the relative decrease in stiffness of pre- and post-contact stiffness of cylindrical lattice increases. This effect is illustrated in Fig. 20 for amplitude ratio 0.20. For the depth of 5 mm, the pre-contact stiffness of the cylindrical lattice is approximately 11% less than that of the planar lattice while this difference increases to approximately 17% and 20% for depths 7.5 mm and 10 mm respectively. Similarly, the post-topology transformation stiffness is approximately 39% less than that of the planar lattice while this difference increases to approximately 42% and 47% for depths 7.5 mm and 10 mm, respectively.

The difference in stiffness of the transformed topology between the cylindrical and planar lattice is greater than that observed for the initial topology. This difference is due to the presence of twist deformation (out-of-plane flexure of beams) in the cylindrical lattice, as is evident from the reaction moment about the vertical axis of the lattice shown in Fig. 21. The reaction moment is negligible until the topology changes and then increases approximately linearly with compression. However, no such reaction moment is present in the case of the planar lattice. This approximate linear increase in reaction moment after topology change is due to the increased resistance to twist deformation caused by the contact connections.

5.4. Poisson's ratio

Similar to the cylindrical lattice, the planar lattice also exhibits NPR behaviour. Fig. 22 compares a planar lattice with an amplitude
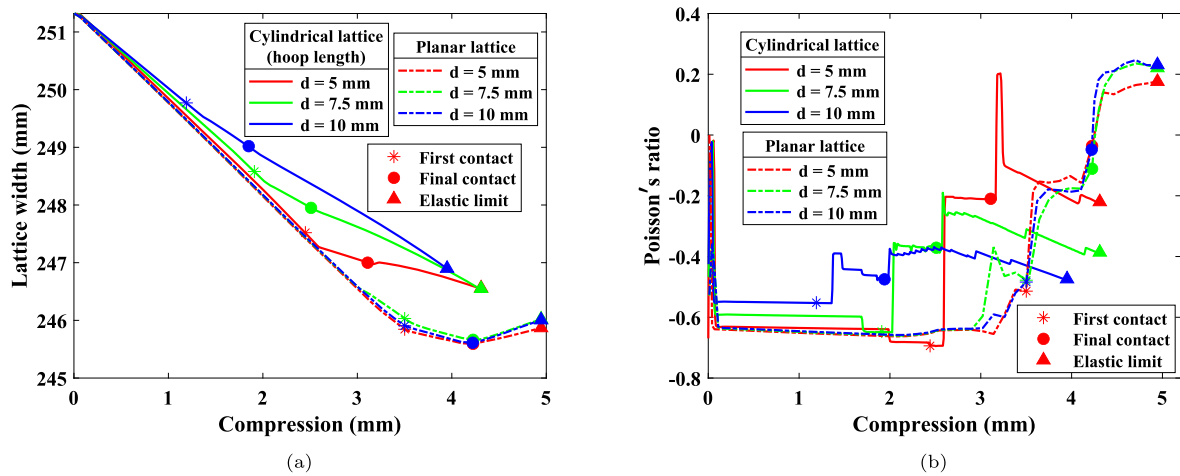
Fig. 22. (a) Lattice width versus compression and (b) Poisson's ratio versus compression of the cylindrical and planar lattices with amplitude ratio 0.20 for various depths, obtained from FE analysis.

ratio of 0.20 and equivalent cylindrical lattices with various depths. Fig. 22a compares the change in lattice width (or hoop length) with compression, and Fig. 22b compares the variation of Poisson's ratio under compression. (The hoop length for the cylindrical lattice is π times the mean diameter, D.)

As shown in Fig. 22a, the width versus compression of the planar lattice is nominally the same for all depths with minor differences observed near the contact regions. The lattice width varies in a piecewise-linear manner. The width decreases with compression until final contact, but at a slower rate after first contact. After final contact, the width increases with compression. Hence, the Poisson's ratio is approximately constant (≈ -0.65) until first contact. Poisson's ratio increases after first contact, remaining approximately constant (≈ -0.16) until final contact. Under further compression, it reaches a positive value of ≈ 0.22 which remains until the elastic limit. In contrast to cylindrical lattices, planar lattices do not display a nonlinear Poisson's ratio after final contact. This absence of nonlinearity is attributed to the absence of out-of-plane flexural behaviour in the vertical beams within the planar arrangement.

In contrast to planar lattices, cylindrical lattices exhibit variations in Poisson's ratio at different depths. Specifically, the Poisson's ratio value increases before the first contact with an increase in the depth of beams, as illustrated in Fig. 22b. This decrease can be attributed to the reduced bending of sinusoidal beams, given their larger cross-sectional area at greater depths. Following the first contact, a significant step-increase occurs, and after the final contact, nonlinear behaviour is observed, as discussed in Section 4.3. However, with an increase in radial depth, the nonlinearity observed in Poisson's ratio after the final contact reduces, suggesting potential tunability for achieving a bimodular NPR response. Nevertheless, unlike planar lattices, the Poisson's ratio of cylindrical lattices remains negative at the elastic limit across all depths.

6. Conclusions

This paper presented a novel concept of passive topology morphing of unit cells within cylindrical sinusoidal lattices. Under sufficient axial compression, self-contact within the unit cells transforms rectangle-like topology into kagome-like topology, resulting in bilinear stiffness and bimodular Poisson's ratio response. Critical geometries exhibiting the desired behaviour were identified by analysing the buckling and compression behaviours of lattices using FE analysis. The load-displacement behaviour observed in FE analysis was validated by experiments performed with MJF 3D-printed prototypes. FE results reveal that the magnitude of the friction coefficient between sinusoidal beams does not

influence the post-contact compressive behaviour before global buckling occurs.

Topology transformation from rectangle-like to kagome-like unit cells results in an approximately four-fold increase in compressive stiffness. The lattice undergoes a step change in auxetic behaviour during topology transformation and exhibits nonlinear Poisson's ratio behaviour afterwards. Geometric parameters, such as amplitude ratio and out-of-plane depth, allow for the tuning of bilinear and bimodular NPR behaviour. By comparison with planar lattices, critical differences between the responses of different global topologies (planar and cylindrical), have been identified. Notably, the cylindrical lattice exhibits bilinear behaviour with smaller amplitude ratios compared to an equivalent planar lattice with the same geometric and material parameters. However, the planar lattice possesses a relatively higher stiffness in its initial topology and also exhibits a greater increase in stiffness (6.88 times) after topology transformation than the cylindrical lattice (4.73 times). The negative Poisson's ratio of planar lattices undergoes step-changes to become positive after topology transformation. The cylindrical lattice presents a different response due to (i) the presence of lateral boundary effects in planar lattices increasing the relative stiffness and (ii) the out-of-plane flexure of the sinusoidal beams in cylindrical lattices reducing the relative stiffness.

The physical insights gained from studying these topology morphing systems could potentially encourage their exploitation in adaptive engineering designs. The compliant behaviour of the lattice in its initial topology can be useful for energy absorption under compression while the membrane behaviour after topology transformation can be useful for load-carrying applications. Due to their NPR and strain-stiffening behaviour, which is similar to that of biological tissues, these structures can also find applications in biomedical devices. Future research could investigate stiffness tailoring to obtain bespoke elastic responses by tuning hierarchical geometric parameters, and also explore the torsional behaviour.

CRediT authorship contribution statement

Venkatesh Sundararaman: Writing – original draft, Visualization, Validation, Project administration, Methodology, Investigation, Conceptualization, Data curation. **Matthew P. O'Donnell:** Writing – review & editing, Supervision. **Isaac V. Chenchiah:** Writing – review & editing, Supervision. **Paul M. Weaver:** Writing – review & editing, Supervision, Funding acquisition.

Declaration of competing interest

Data availability

Data will be made available on request.

Acknowledgements

Appendix A. Supplementary material

Supplementary material related to this article can be found online at https://doi.org/10.1016/j.matdes.2024.112980.

References

[1] B. Ling, K. Wei, Z. Qu, D. Fang, Design and analysis for large magnitudes of programmable Poisson's ratio in a series of lightweight cylindrical metastructures, Int. J. Mech. Sci. 195 (2021) 106220, https://doi.org/10.1016/j.ijmecsci.2020.106220.

[2] D. Han, Y. Zhang, X.Y. Zhang, Y.M. Xie, X. Ren, Lightweight auxetic tubular metamaterials: design and mechanical characteristics, Compos. Struct. 311 (2023) 116849, https://doi.org/10.1016/j.compstruct.2023.116849.

[3] B. Wang, X. Tan, S. Zhu, S. Chen, K. Yao, P. Xu, L. Wang, H. Wu, Y. Sun, Cushion performance of cylindrical negative stiffness structures: analysis and optimization, Compos. Struct. 227 (2019) 111276, https://doi.org/10.1016/j.compstruct.2019.111276.

[4] M. Corsi, S. Bagassi, M.C. Moruzzi, F. Weigand, Additively manufactured negative stiffness structures for shock absorber applications, Mech. Adv. Mat. Struct. 29 (2022) 999–1010, https://doi.org/10.1080/15376494.2020.1801917.

[5] T.R. Giri, R. Mailen, Controlled snapping sequence and energy absorption in multistable mechanical metamaterial cylinders, Int. J. Mech. Sci. 204 (2021) 106541, https://doi.org/10.1016/j.ijmecsci.2021.106541.

[6] N. Ma, Q. Deng, X. Li, Deformation behaviors and energy absorption of composite reentrant honeycomb cylindrical shells under axial load, Materials 14 (2021), https://doi.org/10.3390/ma14237129.

[7] M.O. Doudaran, H. Ahmadi, G. Liaghat, Crushing performance of auxetic tubes under quasi-static and impact loading, J. Braz. Soc. Mech. Sci. Eng. 44 (2022) 230, https://doi.org/10.1007/s40430-022-03539-2.

[8] K.P. Logakannan, J. Rengaswamy, S. Kumar, V. Ramachandran, D. Ruan, Mechanical response of a novel hybrid tube composed of an auxetic outer layer, Thin-Walled Struct. 171 (2022) 108649, https://doi.org/10.1016/j.tws.2021.108649.

[9] X. Ren, Y. Zhang, C.Z. Han, D. Han, X.Y. Zhang, X.G. Zhang, Y.M. Xie, Mechanical properties of foam-filled auxetic circular tubes: experimental and numerical study, Thin-Walled Struct. 170 (2022) 108584, https://doi.org/10.1016/j.tws.2021.108584.

[10] R. Hamzehei, M. Bodaghi, J.A. Iglesias Martinez, Q. Ji, G. Ulliac, M. Kadic, C. Wang, A. Zolfagharian, N. Wu, Parrot beak-inspired metamaterials with friction and interlocking mechanisms 3d/4d printed in micro and macro scales for supreme energy absorption/dissipation, Adv. Eng. Mater. 25 (2023) 2201842, https://doi.org/10.1002/adem.202201842.

[11] H. Ruan, J. Ning, X. Wang, D. Li, Novel tubular structures with negative Poisson's ratio and high stiffness, Phys. Status Solidi B 258 (2020) 2000503, https://doi.org/10.1002/pssb.202000503.

[12] N. Novak, A. Mauko, M. Ulbin, L. Krstulović-Opara, Z. Ren, M. Vesenjak, Development and characterisation of novel three-dimensional axisymmetric chiral auxetic structures, J. Mat. Res. Technol. 17 (2022) 2701–2713, https://doi.org/10.1016/j.jmrt.2022.02.025.

[13] D. Han, Y. Zhang, X.Y. Zhang, Y.M. Xie, X. Ren, Mechanical characterization of a novel thickness gradient auxetic tubular structure under inclined load, Eng. Struct. 273 (2022) 115079, https://doi.org/10.1016/j.engstruct.2022.115079.

[14] J. Plewa, M. Płońska, K. Feliksik, An experimental study of auxetic tubular structures, Materials 15 (2022), https://doi.org/10.3390/ma15155245.

[15] D.T. Farrell, C. McGinn, G.J. Bennett, Extension twist deformation response of an auxetic cylindrical structure inspired by deformed cell ligaments, Compos. Struct. 238 (2020) 111901, https://doi.org/10.1016/j.compstruct.2020.111901.

[16] C. Ma, H. Lei, J. Liang, W. Wu, T. Wang, D. Fang, Macroscopic mechanical response of chiral-type cylindrical metastructures under axial compression loading, Mater. Des. 158 (2018) 198–212, https://doi.org/10.1016/j.matdes.2018.08.022.

[17] D. Goswami, Y. Zhang, S. Liu, O.A. Abdalla, P.D. Zavattieri, R.V. Martinez, Mechanical metamaterials with programmable compression-twist coupling, Smart Mater. Struct. 30 (2020) 015005, https://doi.org/10.1088/1361-665X/abc182.

[18] Y.-B. Wang, H.-T. Liu, Z.-Y. Zhang, Rotation spring: rotation symmetric compression-torsion conversion structure with high space utilization, Compos. Struct. 245 (2020) 112341, https://doi.org/10.1016/j.compstruct.2020.112341.

[19] J.-X. Wang, Q.-S. Yang, Y.-L. Wei, R. Tao, A novel chiral metamaterial with multistability and programmable stiffness, Smart Mater. Struct. 30 (2021) 065006, https://doi.org/10.1088/1361-665X/abf994.

[20] H. Wang, C. Zhang, Q.-H. Qin, Y. Bai, Tunable compression-torsion coupling effect in novel cylindrical tubular metamaterial architected with boomerang-shaped tetrachiral elements, Mater. Today Commun. 31 (2022) 103483, https://doi.org/10.1016/j.mtcomm.2022.103483.

[21] V. Vasiliev, A. Razin, Anisogrid composite lattice structures for spacecraft and aircraft applications, Compos. Struct. 76 (2006) 182–189, https://doi.org/10.1016/j.compstruct.2006.06.025.

[22] C. McHale, R. Telford, P.M. Weaver, Morphing lattice boom for space applications, Composites, Part B, Eng. 202 (2020) 108441, https://doi.org/10.1016/j.compositesb.2020.108441.

[23] C. McHale, D.A. Hadjiloizi, P.M. Weaver, Toroidal deployment of morphing cylindrical lattices, Compos. Struct. 276 (2021) 114577, https://doi.org/10.1016/j.compstruct.2021.114577.

[24] C. McHale, P.M. Weaver, Morphing composite cylindrical lattices with enhanced bending stiffness, Mater. Des. 222 (2022) 111056, https://doi.org/10.1016/j.matdes.2022.111056.

[25] M. Doshi, X. Ning, Instability of metamaterial-based thin cylindrical shells under axial compression, J. Appl. Mech. 91 (2024), https://doi.org/10.1115/1.4063898.

[26] Y. Wang, L. Wang, Z. dong Ma, T. Wang, A negative Poisson's ratio suspension jounce bumper, Mater. Des. 103 (2016) 90–99, https://doi.org/10.1016/j.matdes.2016.04.041.

[27] X. Ren, D. Han, L. Sun, X.G. Zhang, W. Jiang, Z. Tao, Y.M. Xie, F. Yang, G.X. Lu, Experimental and numerical investigations of aluminum foam-filled auxetic circular tubular metamaterials with elliptical cells, Constr. Build. Mater. 374 (2023) 130900, https://doi.org/10.1016/j.conbuildmat.2023.130900.

[28] M.N. Ali, I.U. Rehman, An auxetic structure configured as oesophageal stent with potential to be used for palliative treatment of oesophageal cancer; development and in vitro mechanical analysis, J. Mater. Sci., Mater. Med. 22 (2011) 2573–2581, https://doi.org/10.1007/s10856-011-4436-y.

[29] M.N. Ali, J.J. Busfield, I.U. Rehman, Auxetic oesophageal stents: structure and mechanical properties, J. Mater. Sci., Mater. Med. 25 (2014) 527–553, https://doi.org/10.1007/s10856-013-5067-2.

[30] L.C. Geng, X.L. Ruan, W.W. Wu, R. Xia, D.N. Fang, Mechanical properties of selective laser sintering (sls) additive manufactured chiral auxetic cylindrical stent, Exp. Mech. 59 (2019) 913–925, https://doi.org/10.1007/s11340-019-00489-0.

[31] H. Jiang, H. Ziegler, Z. Zhang, H. Zhang, L. Le Barbenchon, S. Atre, Y. Chen, 3d printed tubular lattice metamaterials for mechanically robust stents, Composites, Part B, Eng. 236 (2022) 109809, https://doi.org/10.1016/j.compositesb.2022.109809.

[32] H. Jiang, H. Ziegler, Z. Zhang, S. Atre, Y. Chen, Bending behavior of 3d printed mechanically robust tubular lattice metamaterials, Addit. Manuf. 50 (2022) 102565, https://doi.org/10.1016/j.addma.2021.102565.

[33] M.F. Simons, K.M. Digumarti, A.T. Conn, J. Rossiter, Tiled auxetic cylinders for soft robots, in: 2019 2nd IEEE International Conference on Soft Robotics (RoboSoft), 2019, pp. 62–67.

[34] D. Goswami, S. Liu, A. Pal, L.G. Silva, R.V. Martinez, 3d-architected soft machines with topologically encoded motion, Adv. Funct. Mater. 29 (2019) 1808713, https://doi.org/10.1002/adfm.201808713.

[35] Y. Dikici, H. Jiang, B. Li, K.A. Daltorio, O. Akkus, Piece-by-piece shape-morphing: engineering compatible auxetic and non-auxetic lattices to improve soft robot performance in confined spaces, Adv. Eng. Mater. 24 (2022) 2101620, https://doi.org/10.1002/adem.202101620.

[36] C. Luo, C.Z. Han, X.Y. Zhang, X.G. Zhang, X. Ren, Y.M. Xie, Design, manufacturing and applications of auxetic tubular structures: a review, Thin-Walled Struct. 163 (2021) 107682, https://doi.org/10.1016/j.tws.2021.107682.

[37] H. Wang, M. Naghavi, C. Allen, R.M. Barber, Z.A. Bhutta, A. Carter, D.C. Casey, F.J. Charlson, A.Z. Chen, M.M. Coates, et al., Global, regional, and national life expectancy, all-cause mortality, and cause-specific mortality for 249 causes of death, 1980–2015: a systematic analysis for the global burden of disease study 2015, Lancet 388 (2016) 1459–1544, https://doi.org/10.1016/S0140-6736(16)31012-1.

[38] S. Bhullar, A.M. Hewage, A. Alderson, K. Alderson, M.B. Jun, Influence of negative Poisson's ratio on stent applications, Adv. Mater. 2 (2013) 42–47, https://doi.org/10.11648/j.am.20130203.14.

[39] Q. Wang, G. Fang, Y.-H. Zhao, J. Zhou, Improvement of mechanical performance of bioresorbable magnesium alloy coronary artery stents through stent pattern redesign, Appl. Sci. 8 (2018), https://doi.org/10.3390/app8122461.

[40] X. Lachenal, P.M. Weaver, S. Daynes, Multi-stable composite twisting structure for morphing applications, Proc. R. Soc. A, Math. Phys. Eng. Sci. 468 (2012) 1230–1251, https://doi.org/10.1098/rspa.2011.0631.

[41] A. Pirrera, X. Lachenal, S. Daynes, P.M. Weaver, I.V. Chenchiah, Multi-stable cylindrical lattices, J. Mech. Phys. Solids 61 (2013) 2087–2107, https://doi.org/10.1016/j.jmps.2013.07.008.

[42] M.D.X. Dixon, M.P. O'Donnell, A. Pirrera, I.V. Chenchiah, Bespoke extensional elasticity through helical lattice systems, Proc. R. Soc. A, Math. Phys. Eng. Sci. 475 (2019) 20190547, https://doi.org/10.1098/rspa.2019.0547.

[43] S. Linß, P. Gräser, T. Räder, S. Henning, R. Theska, L. Zentner, Influence of geometric scaling on the elasto-kinematic properties of flexure hinges and compliant mechanisms, Mech. Mach. Theory 125 (2018) 220–239, https://doi.org/10.1016/j.mechmachtheory.2018.03.008.

[44] G. Arena, R.M.J. Groh, A. Brinkmeyer, R. Theunissen, P.M. Weaver, A. Pirrera, Adaptive compliant structures for flow regulation, Proc. R. Soc. A, Math. Phys. Eng. Sci. 473 (2017) 20170334, https://doi.org/10.1098/rspa.2017.0334.

[45] S. Shan, S.H. Kang, J.R. Raney, P. Wang, L. Fang, F. Candido, J.A. Lewis, K. Bertoldi, Multistable architected materials for trapping elastic strain energy, Adv. Mater. 27 (2015) 4296–4301, https://doi.org/10.1002/adma.201501708.

[46] Z. Vangelatos, G.X. Gu, C.P. Grigoropoulos, Architected metamaterials with tailored 3d buckling mechanisms at the microscale, Extrem. Mech. Lett. 33 (2019) 100580, https://doi.org/10.1016/j.eml.2019.100580.

[47] Z. Meng, M. Liu, Y. Zhang, C.Q. Chen, Multi-step deformation mechanical metamaterials, J. Mech. Phys. Solids 144 (2020) 104095, https://doi.org/10.1016/j.jmps.2020.104095.

[48] M.A. Wagner, T.S. Lumpe, T. Chen, K. Shea, Programmable, active lattice structures: unifying stretch-dominated and bending-dominated topologies, Extrem. Mech. Lett. 29 (2019) 100461, https://doi.org/10.1016/j.eml.2019.100461.

[49] M.A. Wagner, F. Schwarz, N. Huber, L. Geistlich, H. Galinski, R. Spolenak, Deformation-induced topological transitions in mechanical metamaterials and their application to tunable non-linear stiffening, Mater. Des. 221 (2022) 110918, https://doi.org/10.1016/j.matdes.2022.110918.

[50] V. Sundararaman, M.P. O'Donnell, I.V. Chenchiah, G. Clancy, P.M. Weaver, Stiffness tailoring in sinusoidal lattice structures through passive topology morphing using contact connections, Mater. Des. 226 (2023) 111649, https://doi.org/10.1016/j.matdes.2023.111649.

[51] L. Wu, D. Pasini, In situ switchable local resonance in elastic metamaterials through bistable topological transformation, Appl. Phys. Lett. 122 (2023) 221702, https://doi.org/10.1063/5.0152525.

[52] L. Wu, D. Pasini, Topological transformation with emerging zero modes in multistable metamaterials for reprogrammable flexural stiffness, Phys. Rev. Appl. 19 (2023) L061001, https://doi.org/10.1103/PhysRevApplied.19.L061001.

[53] L. Wu, D. Pasini, In situ activation of snap-through instability in multi-response metamaterials through multistable topological transformation, Adv. Mater. 35 (2023) 2301109, https://doi.org/10.1002/adma.202301109.

[54] V. Sundararaman, C. McHale, M.P. O'Donnell, I.V. Chenchiah, P.M. Weaver, Adaptive stiffness in lattice metastructures through tensile-buckling inspired topology morphing, Int. J. Solids Struct. (2023) 112637, https://doi.org/10.1016/j.ijsolstr.2023.112637.

[55] Y. Sha, L. Jiani, C. Haoyu, R.O. Ritchie, X. Jun, Design and strengthening mechanisms in hierarchical architected materials processed using additive manufacturing, Int. J. Mech. Sci. 149 (2018) 150–163, https://doi.org/10.1016/j.ijmecsci.2018.09.038.

[56] J. Deng, X. Li, Z. Liu, Z. Wang, S. Li, Compression behavior of fcc- and bcb-architected materials: theoretical and numerical analysis, Acta Mech. 232 (2021) 4133–4150, https://doi.org/10.1007/s00707-021-02953-2.

[57] C. Guo, D. Zhao, Z. Liu, Q. Ding, H. Gao, Q. Yan, Y. Sun, F. Ren, The 3d-printed honeycomb metamaterials tubes with tunable negative Poisson's ratio for high-performance static and dynamic mechanical properties, Materials 14 (2021), https://doi.org/10.3390/ma14061353.

[58] X. Cheng, Y. Zhang, X. Ren, D. Han, W. Jiang, X.G. Zhang, H.C. Luo, Y.M. Xie, Design and mechanical characteristics of auxetic metamaterial with tunable stiffness, Int. J. Mech. Sci. 223 (2022) 107286, https://doi.org/10.1016/j.ijmecsci.2022.107286.

[59] H. Lu, X. Wang, T. Chen, Design and quasi-static responses of a hierarchical negative Poisson's ratio structure with three Plateau stages and three-step deformation, Compos. Struct. 291 (2022) 115591, https://doi.org/10.1016/j.compstruct.2022.115591.

[60] T. Chen, M. Pauly, P.M. Reis, A reprogrammable mechanical metamaterial with stable memory, Nature 589 (2021) 386–390, https://doi.org/10.1038/s41586-020-03123-5.

[61] S. Li, B. Deng, A. Grinthal, A. Schneider-Yamamura, J. Kang, R.S. Martens, C.T. Zhang, J. Li, S. Yu, K. Bertoldi, et al., Liquid-induced topological transformations of cellular microstructures, Nature 592 (2021) 386–391, https://doi.org/10.1038/s41586-021-03404-7.

[62] S. Hyun, S. Torquato, Optimal and manufacturable two-dimensional, Kagome-like cellular solids, J. Mater. Res. 17 (2002) 137–144, https://doi.org/10.1557/JMR.2002.0021.

[63] Abaqus Documentatio, Simulia user assistance, https://help.3ds.com, 2020. (Accessed 8 December 2022).

[64] HUBS, HP 3D high reusability pa 12, https://www.hubs.com/3d-printing/plastic/nylon/hp-pa-12, 2018. (Accessed 31 August 2023).

[65] H. Yang, W. Jiang, M. Li, L. Ma, Multi-material 3d double-v metastructures with tailorable Poisson's ratio and thermal expansion, Int. J. Mech. Sci. 210 (2021) 106733, https://doi.org/10.1016/j.ijmecsci.2021.106733.

[66] HP (Hewlett-Packard), HP multi jet fusion technology, https://www.hp.com/us-en/printers/3d-printers/products/multi-jet-technology.html. (Accessed 31 August 2023), 2023.

[67] H.J. O'Connor, A.N. Dickson, D.P. Dowling, Evaluation of the mechanical performance of polymer parts fabricated using a production scale multi jet fusion printing process, Addit. Manuf. 22 (2018) 381–387, https://doi.org/10.1016/j.addma.2018.05.035.